Removal of Spurious Coherence in MEG Source-Space Coherence Analysis

Kensuke Sekihara*, *Fellow, IEEE*, Julia P. Owen, Stephan Trisno, and Srikantan S. Nagarajan, *Senior Member, IEEE*

***Abstract*—Source-space coherence analysis has become a popular method to estimate functional connectivity based on MEG/EEG. Source-space analysis involves solving the inverse problem, estimating the time courses of specific brain regions, and then examining the coherence between activities at different brain regions. However, source-space coherence analysis can be confounded by spurious coherence caused due to the leakage properties of the inverse algorithm employed. Such spurious coherence is typically manifested as an artifactual large peak around the seed voxel, called seed blur, in the resulting coherence images. This seed blur often obscures important details of brain interactions. This paper proposes the use of the imaginary part of the coherence to remove the spurious coherence caused by the leakage of an imaging algorithm. We present a theoretical analysis that explains how the use of imaginary part can remove this spurious coherence. We then present results from both computer simulations and experiments using resting-state MEG data which demonstrate the validity of our analysis.**

***Index Terms*—Bioelectromagnetism, coherence analysis, functional connectivity, magnetoencephalography (MEG), MEG source imaging, source coherence.**

I. Introduction

THERE has been tremendous interest in estimating the functional connectivity of neuronal oscillations across brain regions based on electromagnetic measurements such as magnetoencephalography (MEG) and electroencephalography (EEG). However, prior studies using EEG or MEG have largely employed sensor-space analysis, in which brain interactions have been analyzed using raw sensor recordings [1]–[3]. In sensor-space analysis, the field spread across many sensors from a single brain region leads to uncertainties in interpreting the estimation results of brain interactions, as pointed out in [4].

Recently, a number of studies have begun to use source-space analysis. In source-space analysis, voxel time courses are first estimated by solving the inverse problem and brain interactions are then analyzed using those estimated voxel time courses [4]–[8]. Although a certain degree of inaccuracy exists in the source inversion process, the source-space analysis has the potential of providing more accurate information regarding which brain regions are functionally coupled.

Either in sensor- or source-space analysis, some kind of a measure for the interaction, called a connectivity metric, must be computed. Among existing measures a widely used representative measure is coherence [5]–[7], [9]–[11]. In source-space coherence analysis, a typical procedure involves first setting a reference point, called the seed point, and computing the coherence between the time courses from the seed point and another voxel's location, referred to as the target location in this paper. By scanning through all target locations in a brain, a 3-D mapping of source coherence, namely a source-coherence image, with respect to the seed location can be obtained.

A serious problem in source-coherence imaging arises from the spurious coherence caused by the leakage of an inverse algorithm, and such leakages are more or less inevitable in any inverse algorithm [12]. One representative ramification of this spurious coherence is an artifactual large peak around the seed voxel, called seed blur, in the resulting coherence image. Quite often, the seed blur dominates the resultant coherence images, and obscures important details of the brain interactions. Examples of the seed blur are shown in our computer simulations and experiments using resting-state MEG data.

To remove such spurious coherence, this paper proposes the use of the imaginary part of coherence, which is called the imaginary coherence. The use of imaginary coherence was originally proposed by Nolte *et al.* [13] to remove the spurious coherence caused by the volume conduction in EEG sensor-space coherence analysis. This paper extends their sensor-space analysis of imaginary coherence to source-space coherence analysis, and presents a detailed theoretical analysis that explains how the use of imaginary coherence leads to the removal of the spurious coherence caused by the leakage of source imaging algorithms. The validity of our analysis is then demonstrated by our computer simulation and by experiments using resting-state MEG data.

II. Method

A. Source-Space Coherence Analysis

Source-space coherence analysis (or source-coherence imaging) requires a two-step procedure. In the first step, voxel time courses are estimated using an inverse algorithm. In the second step, the coherence measure is computed using the voxel time courses estimated in the first step. In this paper, the coherence

Manuscript received April 25, 2011; revised June 8, 2011; accepted July 3, 2011. Date of publication August 4, 2011; date of current version October 19, 2011. The work of K. Sekihara was supported by the Ministry of Education, Science, Culture and Sports, Japan, under Grant 20500394 and Grant 22659210. The work of S. S. Nagarajan was supported by the National Institute of Health under Grant R01-DC004855-01A1 and Grant R01-NS006435. *Asterisk indicates corresponding author.*

*K. Sekihara is with the Department of Systems Design and Engineering, Tokyo Metropolitan University, Tokyo 191-0065, Japan (e-mail: k-sekihara@nifty.com).

J. P. Owen, S. Trisno, and S. S. Nagarajan are with the Department of Radiology and Biomedical Imaging, Biomagnetic Imaging Laboratory, University of California, San Francisco, CA 94143 USA (e-mail: juliapowen@gmail.com; strisno@berkeley.edu; srikantan.nagarajan@ucsf.edu).

Color versions of one or more of the figures in this paper are available online at http://ieeexplore.ieee.org.

Digital Object Identifier 10.1109/TBME.2011.2162514

is computed between the time courses from the seed voxel and from each of the target voxel. Let us define the time course from the seed voxel as $u_S(t)$ and the time course from a target voxel as $u_T(t)$, and let the spectra of the seed and the target voxels be $\sigma_S(f)$ and $\sigma_T(f)$, respectively.

The coherence $\eta(f)$ is obtained by computing the correlation of these spectra

$$\eta(f) = \frac{\langle \sigma_T(f)\sigma_S^*(f)\rangle}{\sqrt{\langle|\sigma_T(f)|^2\rangle\langle|\sigma_S(f)|^2\rangle}} \tag{1}$$

where the superscript $*$ indicates the complex conjugate, and the bracket $\langle\cdot\rangle$ indicates the ensemble average. In practical applications, this ensemble average is computed by averaging across multiple trials. When only a single continuous dataset is measured, the single dataset is divided into many trials and coherence is obtained by averaging across these trials.

In conventional source-coherence imaging, the magnitude coherence $|\eta(f)|$ is computed and mapped by scanning through the target voxels. It is, however, apparent from (1) that if the seed and target spectra contain common components that do not result from true brain interactions, then the magnitude coherence may contain spurious components. When coherence is computed between estimated voxel time courses, the leakage of the imaging algorithm used is a major source of such spurious coherence.

B. Leakage Effects of Imaging Algorithms

1) Leakage Effects in the Magnitude Coherence: The estimated source time courses at the seed voxel $\widehat{u}_S(t)$ and at the target voxel $\widehat{u}_T(t)$ can be expressed as

$$\widehat{u}_S(t) = u_S(t) + d_1 u_T(t) + c_S(t) \tag{2}$$

and

$$\widehat{u}_T(t) = u_T(t) + d_2 u_S(t) + c_T(t) \tag{3}$$

where $u_S(t)$ and $u_T(t)$ are the true source time courses of the seed and the target locations, respectively.[1] In the aforementioned equations, $d_1 u_T(t)$ indicates the leakage of the target signal in the estimated seed signal, and $d_2 u_S(t)$ indicates the leakage of the seed signal in the estimated target signal. The real-valued constants d_1 and d_2 express the relative amount of these leakages.

In the aforementioned equations, $c_S(t)$ and $c_T(t)$ express the interference terms, which may include the leakage from other sources, contributions from external disturbances, and that of the sensor noise. The influence of these interference terms can be considered separately from the influence of the leakage terms in Section V. In the arguments here, we ignore $c_S(t)$ and $c_T(t)$ and the estimated spectra at the seed and target voxels, $\widehat{\sigma}_S(f)$ and $\widehat{\sigma}_T(f)$, are, respectively, expressed as

$$\widehat{\sigma}_S = \sigma_S + d_1\sigma_T \qquad \text{and} \qquad \widehat{\sigma}_T = \sigma_T + d_2\sigma_S \tag{4}$$

where we omit the explicit notation of (f) for simplicity.

[1]In this paper, the estimated values are indicated by $\widehat{\ }$ to distinguish their true values.

The magnitude coherence between the seed and the target voxels is expressed as

$$|\widehat{\eta}| = \left|\frac{\langle\widehat{\sigma}_T\widehat{\sigma}_S^*\rangle}{\sqrt{\langle|\widehat{\sigma}_T|^2\rangle\langle|\widehat{\sigma}_S|^2\rangle}}\right|. \tag{5}$$

Using (4), we have

$$\langle\widehat{\sigma}_T\widehat{\sigma}_S^*\rangle = \langle\sigma_T\sigma_S^*\rangle + d_1\langle|\sigma_T|^2\rangle + d_2\langle|\sigma_S|^2\rangle + d_1 d_2\langle\sigma_S\sigma_T^*\rangle \tag{6}$$

$$\langle|\widehat{\sigma}_T|^2\rangle = \langle|\sigma_S|^2\rangle + d_1^2\langle|\sigma_T|^2\rangle + 2d_1\Re\left(\langle\sigma_T\sigma_S^*\rangle\right) \tag{7}$$

and

$$\langle|\widehat{\sigma}_S|^2\rangle = \langle|\sigma_T|^2\rangle + d_2^2\langle|\sigma_S|^2\rangle + 2d_2\Re\left(\langle\sigma_T\sigma_S^*\rangle\right) \tag{8}$$

where $\Re(\cdot)$ indicates the real part. Therefore, even when there is no true source interaction, i.e., even when $\langle\sigma_T\sigma_S^*\rangle = 0$ and $\langle\sigma_S\sigma_T^*\rangle = 0$, $|\widehat{\eta}|$ has a nonzero value, which is equal to

$$|\widehat{\eta}| = \frac{|d_1\langle|\sigma_T|^2\rangle + d_2\langle|\sigma_S|^2\rangle|}{\sqrt{\left(\langle|\sigma_S|^2\rangle + d_1^2\langle|\sigma_T|^2\rangle\right)\left(\langle|\sigma_T|^2\rangle + d_2^2\langle|\sigma_S|^2\rangle\right)}}. \tag{9}$$

Such spurious coherence is typically manifested as an artifactual large peak around the seed voxel, called seed blur, in the resulting coherence images.

2) Leakage Effects in the Imaginary Coherence: Using (6) and the relationship

$$\langle\sigma_T\sigma_S^*\rangle + \langle\sigma_S\sigma_T^*\rangle = 2\Re\left(\langle\sigma_S\sigma_T^*\rangle\right)$$

the cross spectrum $\langle\widehat{\sigma}_T\widehat{\sigma}_S^*\rangle$ can be expressed as

$$\langle\widehat{\sigma}_T\widehat{\sigma}_S^*\rangle = (1 - d_1 d_2)\langle\sigma_T\sigma_S^*\rangle + d_1\langle|\sigma_T|^2\rangle + d_2\langle|\sigma_S|^2\rangle + 2d_1 d_2\Re\left(\langle\sigma_T\sigma_S^*\rangle\right). \tag{10}$$

By taking the imaginary part of (10), we can derive

$$\Im\left(\langle\widehat{\sigma}_T\widehat{\sigma}_S^*\rangle\right) = (1 - d_1 d_2)\Im\left(\langle\sigma_T\sigma_S^*\rangle\right) \tag{11}$$

where $\Im(\cdot)$ indicates the imaginary part. The aforementioned equation indicates that, aside from the multiplicative constant, the imaginary part of the cross spectrum between the seed and target voxels is equal to $\Im\left(\langle\sigma_T\sigma_S^*\rangle\right)$, which is the imaginary part of the true cross spectrum.

To compute coherence, the cross spectrum $\langle\widehat{\sigma}_T\widehat{\sigma}_S^*\rangle$ is normalized by $\sqrt{\langle|\widehat{\sigma}_T|^2\rangle\langle|\widehat{\sigma}_S|^2\rangle}$. Thus, we obtain the imaginary part of the estimated coherence $\Im(\widehat{\eta})$ as

$$\Im(\widehat{\eta}) = \frac{\Im\left(\langle\widehat{\sigma}_T\widehat{\sigma}_S^*\rangle\right)}{\sqrt{\langle|\widehat{\sigma}_T|^2\rangle\langle|\widehat{\sigma}_S|^2\rangle}} = \frac{(1 - d_1 d_2)\Im\left(\langle\sigma_T\sigma_S^*\rangle\right)}{\sqrt{\langle|\widehat{\sigma}_T|^2\rangle\langle|\widehat{\sigma}_S|^2\rangle}} = \Omega\,\Im(\eta) \tag{12}$$

where $\Im(\eta)$ indicates the true value of the imaginary coherence. Using (7) and (8), Ω is obtained as

$$\Omega = \frac{(1 - d_1 d_2)}{\sqrt{\phi_1\phi_2}} \tag{13}$$

where

$$\phi_1 = 1 + d_1^2\frac{\langle|\sigma_T|^2\rangle}{\langle|\sigma_S|^2\rangle} + 2d_1\frac{\Re\left(\langle\sigma_T\sigma_S^*\rangle\right)}{\langle|\sigma_S|^2\rangle} \tag{14}$$

and

$$\phi_2 = 1 + d_2^2 \frac{\langle |\sigma_S|^2 \rangle}{\langle |\sigma_T|^2 \rangle} + 2d_2 \frac{\Re\left(\langle \sigma_T \sigma_S^* \rangle\right)}{\langle |\sigma_T|^2 \rangle}. \tag{15}$$

Equation (12) shows that when $\Im(\eta) = 0$, we have $\Im(\widehat{\eta}) = 0$, indicating that no spurious coherence has been generated.

However, (12) also indicates that the value of $\Im(\widehat{\eta})$ differs from the true value $\Im(\eta)$, i.e., the amplitude of the estimated imaginary coherence is biased and the bias is represented by Ω, which is called the amplitude bias factor in this paper. Let us calculate the amplitude bias factor assuming a simple scenario in which $d_1 = d_2 = d$ and $\langle |\sigma_S|^2 \rangle = \langle |\sigma_T|^2 \rangle$. Under these assumptions, the bias factor is simplified to

$$\frac{1 + |d|}{1 - |d|} \geq \Omega = \frac{1 - d^2}{1 + d^2 + 2\Re(\eta)d} \geq \frac{1 - |d|}{1 + |d|}. \tag{16}$$

The aforementioned equation shows how the amount of leakage $|d|$ affects the amplitude bias Ω, and it shows that if $|d|$ is small such as $|d| < 0.1$, the amplitude bias is less than 10%. The narrow-band adaptive spatial filter used in our investigation generally has small leakages [12], and thus, this amplitude bias is generally small. We check this fact in our computer simulation.

C. Statistical Thresholding of an Imaginary-Coherence Image

In practical applications, we need to assess the statistical significance of the imaginary coherence. In this paper, the surrogate data method [14], [15] is used for this assessment. In this method, the surrogate voxel spectra are created by multiplying random phases with the original voxel spectra. The surrogate spectra for the seed and the target voxels $\widetilde{\sigma}_S(f)$ and $\widetilde{\sigma}_T(f)$ are expressed as

$$\widetilde{\sigma}_S = \widehat{\sigma}_S e^{2\pi\varepsilon_S} \quad \text{and} \quad \widetilde{\sigma}_T = \widehat{\sigma}_T e^{2\pi\varepsilon_T} \tag{17}$$

where ε_S and ε_T are the uniform random numbers between 0 and 1, and the explicit notation of (f) is again omitted for simplicity. Note that the surrogate spectra have the same original power spectra but the phase relationship is destroyed by multiplying the random phases to the original spectra. The value of the imaginary coherence calculated using the surrogate spectra $\widetilde{\sigma}_S$ and $\widetilde{\sigma}_T$ is expressed as

$$\xi = \frac{\Im\left(\langle \widetilde{\sigma}_T \widetilde{\sigma}_S^* \rangle\right)}{\sqrt{\langle |\widetilde{\sigma}_T|^2 \rangle \langle |\widetilde{\sigma}_S|^2 \rangle}} = \frac{\Im\left(\langle \widehat{\sigma}_T \widehat{\sigma}_S^* e^{2\pi\Delta\varepsilon} \rangle\right)}{\sqrt{\langle |\widehat{\sigma}_T|^2 \rangle \langle |\widehat{\sigma}_S|^2 \rangle}} \tag{18}$$

where $\Delta\varepsilon = \varepsilon_T - \varepsilon_S$. The generation of ξ is repeated with B times, and a total B values of ξ, which are denoted $\xi^1, \xi^2, \ldots, \xi^B$, are obtained. These $\xi^1, \ldots, \xi^B$ can form an empirical null distribution at each target voxel. We then could derive a voxel-by-voxel statistical threshold using this empirical null distribution. However, the statistical threshold derived in this manner does not take the multiple comparisons into account and it generally leads to a situation in which many false-positive voxels arise, i.e., many voxels that contain no brain interaction are found to be interacting. To avoid this problem, the statistical significance is determined using a procedure that takes multiple comparisons into account. For this purpose, we use the maximal statistics [16], [17].

To utilize maximum statistics, the values ξ^β $(\beta = 1, \ldots, B)$ are first standardized and converted into pseudo-t values, such that

$$T^\beta = \frac{\xi^\beta - \bar{\xi}}{\sigma_\xi} \tag{19}$$

where $\bar{\xi}$ and σ_ξ^2 are the average and the variance of ξ^β $(\beta = 1, \ldots, B)$, respectively. Since these $\bar{\xi}$ and σ_ξ^2 are obtained at each target voxel, the values at the jth target voxel are denoted as $\bar{\xi}(j)$ and $\sigma_\xi^2(j)$. The maximum value of T^β obtained at the jth voxel is denoted as $T^{\max}(j)$. Denoting a total number of voxels N_V, we have $T^{\max}(1), \ldots, T^{\max}(N_V)$ to form the null distribution. We then sort these values in an increasing order

$$T^{\max}(\tilde{1}) \leq T^{\max}(\tilde{2}) \leq \cdots \leq T^{\max}(\tilde{N}_V)$$

where $T^{\max}(\tilde{k})$ is the kth minimum value. We set the level of the statistical significance to α, and choose $T^{\max}(\tilde{p})$ where $\tilde{p} = \lceil \alpha N_V \rceil$ where $\lceil \alpha N_V \rceil$ indicates the maximum integer not greater than αN_V. The threshold value for the jth voxel $\xi^{\mathrm{th}}(j)$ is derived as

$$\xi^{\mathrm{th}}(j) = T^{\max}(\tilde{p})\sigma_\xi(j) + \bar{\xi}(j). \tag{20}$$

We evaluate, at the jth voxel, the statistical significance of the imaginary coherence by comparing $|\Im(\widehat{\eta})|$ with $|\xi^{\mathrm{th}}(j)|$. When $|\Im(\widehat{\eta})| > |\xi^{\mathrm{th}}(j)|$, the imaginary coherence at the jth voxel $\Im(\widehat{\eta})$ is considered to be statistically significant. Conversely, if $|\xi^{\mathrm{th}}(j)| > |\Im(\widehat{\eta})|$, $\Im(\widehat{\eta})$ is not considered to be statistically significant, and it is set to 0.

III. Computer Simulation

A. Data Generation

Computer simulations were performed to verify the arguments in Section II-B. In our simulations, we used a sensor alignment of the 275-sensor array from the Omega (VMS Medtech Ltd., Coquitlam, BC, Canada) neuromagnetometer. A single vertical plane ($x = 0$ cm) was assumed at the middle of the whole-head sensor array, and three sources were assumed to exist on this plane. The source–sensor configuration and the coordinate system are depicted in Fig. 1. The (y, z) coordinates of the three sources were $(-1.0, 9.5)$, $(1.5, 10.0)$, and $(1.0, 7.5)$ cm, respectively.

Multiple-trial measurements were simulated, in which a total of 120 trial recordings were generated. Each trial consists of 600 time points where the sampling interval was assumed to be 2 ms. The time courses of the three sources had the same shape with trial-to-trial time jitters. The time jitter between the first and second sources and the jitter between the second and the third sources were both generated using Gaussian random numbers with a standard deviation equal to 15 time points. There is a 50-time-point mean delay between the time courses of the first and the second sources, and also between those of the second and the third sources. Here, the amount of jitter controls the value of coherence, and setting the jitters in the aforementioned manner results in the following values: $|\Im(\eta_{1,2})| = 0.27$ and $|\Im(\eta_{2,3})| = 0.23$ where $\eta_{1,2}$ indicates the coherence between

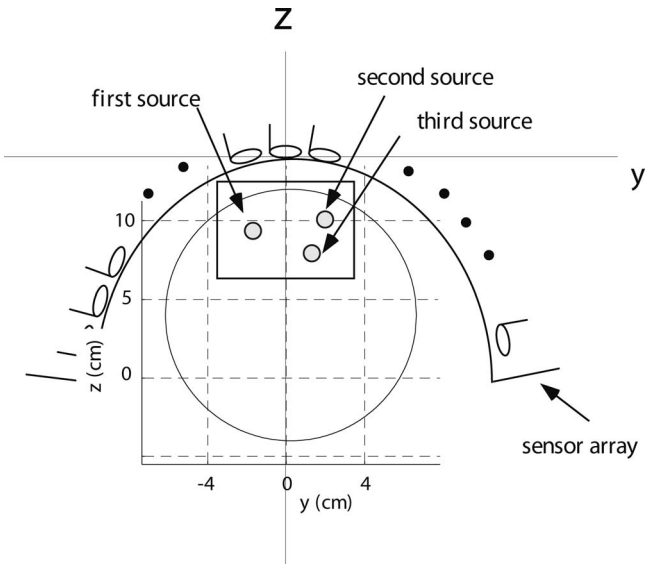

Fig. 1. Coordinate system and source–sensor configuration used in the computer simulation. The coordinate origin was set at the center of the sensor coil located at the center of the array. The plane at $x = 0$ cm is shown. The large circle shows the cross section of the sphere used for the forward calculation, and the small circles show the locations of the three sources. The square shows the region for which reconstruction results are shown in Figs. 3–5.

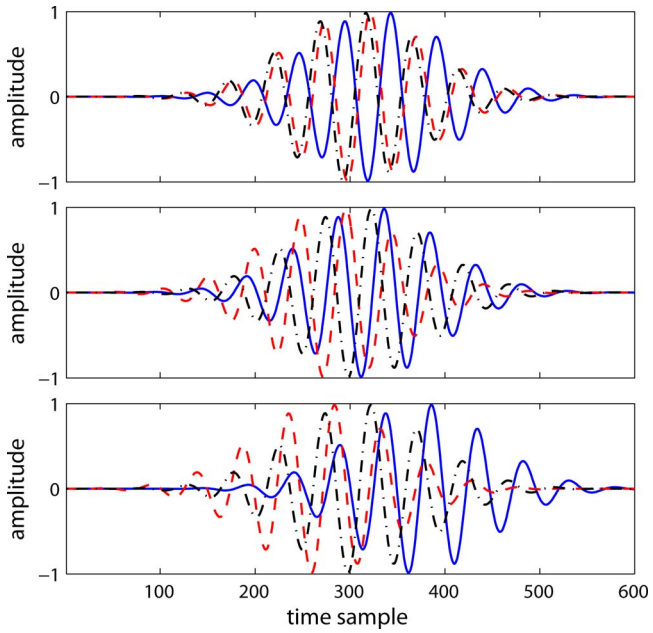

Fig. 2. Time courses assigned to the three sources in the computer simulation. The time courses in the top, middle, and bottom panels are those for the first, second, and the third sources, respectively. These time courses have trial-to-trial time jitters, and the time courses in the first three trials are shown. The solid, broken, and dashed-dotted lines, respectively, show the time courses for the first, second, and third trials.

the first and second sources and $\eta_{2,3}$ that between the second and third sources. Also, $\Im(\eta_{1,2})$ and $\Im(\eta_{2,3})$ indicate the imaginary parts of these coherence values. The source time courses in the first three trials are shown in Fig. 2.

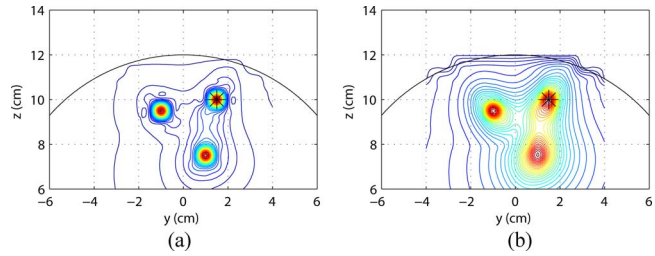

Fig. 3. Results of reconstructing source power distribution on the plane $x = 0$ cm. (a) SIR was set equal to 4.0. (b) SIR was set equal to 0.25. Asterisks show the location of the seed that was set for computing the coherence images shown in Fig. 4.

Defining the jth-source time course given as $u_j(t)$, the signal magnetic recordings $\boldsymbol{b}_s(t)$ were computed using

$$\boldsymbol{b}_s(t) = \sum_{j=1}^{3} A_j u_j(t) \boldsymbol{l}_j \tag{21}$$

where $\boldsymbol{l}_j$ is the lead field vector of the jth source and A_j is its amplitude. Here, the powers of the three sources were set equal in the sensor domain, i.e., the relationship

$$A_1^2 \|\boldsymbol{l}_1\|^2 = A_2^2 \|\boldsymbol{l}_2\|^2 = A_3^2 \|\boldsymbol{l}_3\|^2$$

held. The lead field was calculated using the spherical homogeneous conductor model [18] with the sphere origin set to $(0, 0, 4)$ cm.

The simulated sensor recordings $\boldsymbol{b}(t)$ were generated by adding spontaneous MEG signal to the computed signal recordings $\boldsymbol{b}_s(t)$, such that

$$\boldsymbol{b}(t) = \boldsymbol{b}_s(t) + \gamma \boldsymbol{b}_I(t) \tag{22}$$

where $\boldsymbol{b}_I(t)$ is the spontaneous MEG measured using the same 275 whole-head sensor array, and γ is a constant that controls the signal-to-interference ratio (SIR) of the simulated sensor recordings. In our computer simulations, an SIR was set equal to 4.0 and 0.25, where SIR is defined as the ratio of the average signal power $\langle \|\boldsymbol{b}_s(t)\|^2 \rangle$ to the average interference power $\langle \|\boldsymbol{b}_I(t)\|^2 \rangle$. Note that the coherence analysis is usually performed using non-averaged trial data. Therefore, an SIR of 4.0 is considered a significantly high SIR and the SIR of 0.25 can be considered a typical SIR for non-averaged trials.

B. *Source-Coherence Imaging*

The voxel time-course estimation was performed using the narrow-band adaptive spatial filter [12], [19] with a data covariance matrix obtained with a frequency band between 8 and 12 Hz. This is because the spectra of source time courses are bandlimited to this bandwidth. Reconstructed source power images on the plane $x = 0$ cm are shown in Fig. 3 for both SIR cases. The reconstructed images show that the three sources are resolved for the both SIR cases. We then set a seed point at the location of the second source to compute coherence images. The seed point is marked by asterisks in Fig. 3.

The resultant coherence images are shown in Fig. 4. To obtain these results, statistical thresholding using the surrogate data

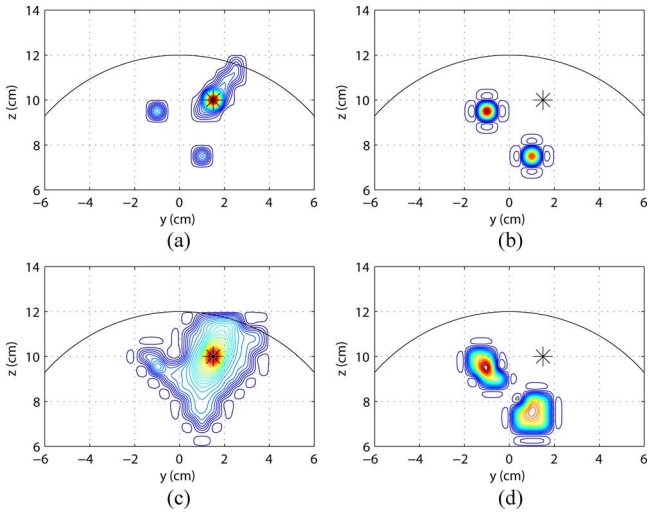

Fig. 4. Results of imaging the source coherence on the plane $x = 0$ cm. The seed was set at the second source location indicated by the asterisk. (a) Magnitude-coherence image when SIR was set equal to 4.0. (b) Imaginary-coherence image when SIR was set equal to 4.0. (c) Magnitude-coherence image when SIR was set equal to 0.25. (d) Imaginary-coherence image when SIR was set equal to 0.25. Statistical thresholding using the surrogate data method described in Section II-C was applied with the number of surrogate datasets to 200 and the level of the statistical significance set to 0.99.

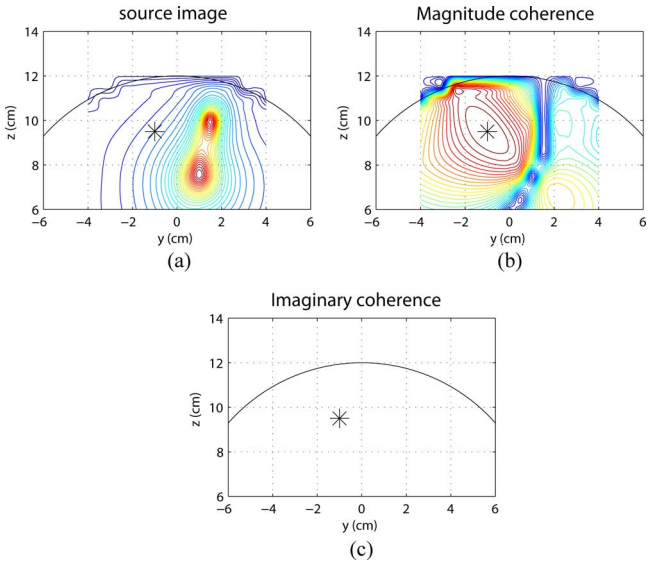

Fig. 5. Results of imaging the source coherence on the plane $x = 0$ cm when the seed was set at a location where no active source existed. The first source was made inactive, and the seed was set at the first source location indicated by the asterisks. (a) Reconstructed source power distribution. (b) Magnitude-coherence image. (c) Imaginary-coherence image. Statistical thresholding using the surrogate data method described was applied with the number of surrogate datasets to 200 and the level of the statistical significance set to 0.99.

method described in Section II-C was applied. Here, the number of surrogate datasets B was set to 200, and the level of the statistical significance α was set to 0.99. The upper panels in Fig. 4(a) and (b) show the results for the case of the SIR equal to 4.0, and the lower panels in Fig. 4(c) and (d) show the results for the case of the SIR equal to 0.25. Also, the left panels in Fig. 4(a) and (c) show the magnitude-coherence images and the right panels in Fig. 4(b) and (d) show the imaginary-coherence images.

When the SIR is equal to 4.0, i.e., when the SIR is very high, the magnitude-coherence image [see Fig. 4(a)] manages to show the first and the third sources, although a large seed blur exists at the second source location. That is, the two sources interacting with the second source can be observed in spite of the existence of the seed blur when the SIR is very high. In the imaginary-coherence image [see Fig. 4(b)], the intensity of the seed blur is much reduced, and the first and the third sources, which interact with the second source, are clearly shown.

When the SIR is equal to 0.25, i.e., when the SIR is typical of coherence analysis, the seed blur dominates and it obscures the other sources in the magnitude-coherence image [see Fig. 4(c)]. Thus, it is difficult to obtain information on the interacting sources from the magnitude-coherence image. On the contrary, in the imaginary-coherence image [see Fig. 4(d)], the intensity of the seed blur is much reduced and the two sources that interact with the second source can clearly be observed.

The narrow-band adaptive spatial filter generally has a small leakage [12]. In this computer simulation, the leakage constants d_1 and d_2 are approximately equal to 0.01 between the first and the second sources, and also between the second and the third sources. Therefore, the bias factor Ω in (16) is nearly equal to 1, and the amplitude bias should be small. Actually, in our computer simulation, the estimated imaginary coherence, $|\Im(\widehat{\eta}_{1,2})|$ and $|\Im(\widehat{\eta}_{3,2})|$ are equal to 0.275 and 0.23 when the SIR was set to 4, and 0.26 and 0.21 when the SIR was set to 0.25. These values of the estimated imaginary coherence are very close to their true values, $|\Im(\eta_{1,2})| = 0.27$ and $|\Im(\eta_{2,3})| = 0.23$, and thus, the amplitude bias is not evident in this computer simulation.

Next, we performed computer simulation in which no source activity existed at the seed location. Here, the first source was made inactive and the seed was set at the first source location. The results of the source power reconstruction in this case are shown in Fig. 5(a). The results contain the second and the third sources but do not contain the first source. The seed location is indicated by the asterisk at the first source location. The thresholded magnitude-coherence and the imaginary-coherence images are shown in Fig. 5(b) and (c). The magnitude-coherence image [see Fig. 5(b)] shows a large blurred peak at the seed location, as if the large region surrounding the seed location is synchronously active. This large region represents the spurious coherence expressed in (9). The imaginary-coherence image [see Fig. 5(c)], however, shows no activity.

IV. Experiments With Resting-State MEG Data

We performed source-coherence imaging using resting-state MEG data. Three healthy subjects participated in the study, which was approved by the ethics committee of University of California, San Francisco. The data were acquired using a 275-channel CTF Omega 2000 whole-head MEG system (VSM MedTech Ltd.). When collecting the data, subjects were laid down with their eyes closed, and 60-s-long single continuous datasets were acquired with a 1200 Hz sampling rate. The

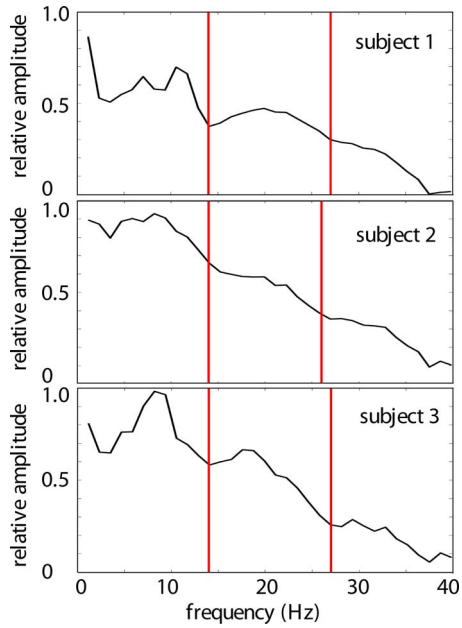

Fig. 6. Power spectra of the sensor data for three subjects. The power spectrum is the mean power spectrum across all sensors and all trials. The two red lines denote the beta range used for the coherence analysis.

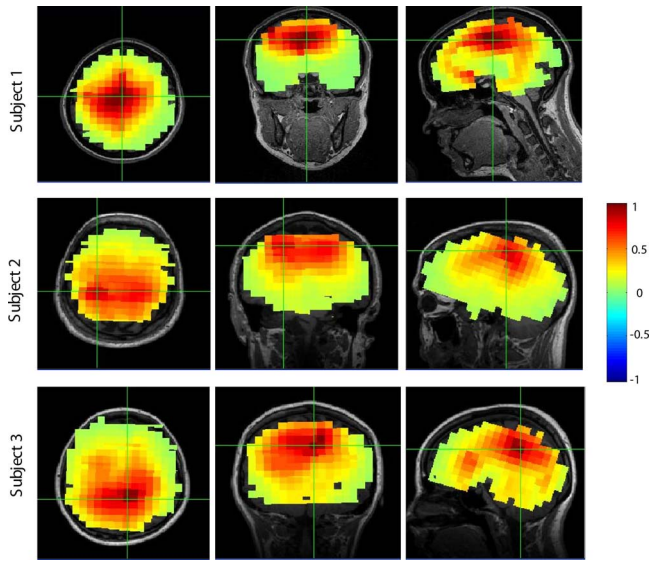

Fig. 7. Results of source power reconstruction for the three-subject cases. The results from the first, second, and third subjects are, respectively, shown in the upper, middle, and bottom rows. The reconstructed voxel power is computed using the squared mean of the voxel time course. The normalized voxel power is color-coded according to the color bar, and overlaid onto each subject's MRI. Three orthogonal MR slices at the voxel with the maximum intensity are shown.

single trial data were divided into 2-s-long trials with half overlap, resulting in a total of 60 trials. The power spectra of the sensor data for three-subject cases are shown in Fig. 6. Each power spectrum was computed using the mean power spectrum across all sensors and all trials.

The voxel time courses were estimated using the narrow-band adaptive spatial filter [12], [19] with the frequency band tuned to the individual subjects' beta band, approximately between 14 and 27 Hz. The two red lines in Fig. 6 denote the beta range for each individual subject used for the narrow-band spatial filter. The source reconstruction was performed using the NUTMEG toolbox [20], and the results are shown in Fig. 7 for the three-subject cases. In these results, the reconstructed voxel power, which is the squared mean of the voxel time course, was mapped, and three orthogonal MR slices at the voxel with the maximum intensity are shown. In all three-subject cases, a large blurred peak exists in a middle, posterior region, and the peak maxima are not necessarily located near primary motor areas.

We then performed source-coherence imaging by setting seed voxels at the left motor area. To obtain seed voxels, we selected all the voxels whose location was determined to be within the precentral gyrus. These location labels were obtained by normalizing the subjects MRI to the Montreal Neurological Institute template brain. We then computed the centroid for these voxels and selected the nine nearest voxels to the centroid, resulting in ten seed voxels in the left precentral gyrus for each subject. The seed voxels for each individual subject are shown in the two leftmost columns of Fig. 8.

We computed the magnitude and imaginary coherence between the seed voxels and the remaining voxels, resulting in ten coherence images corresponding to each of the ten seed voxels. The final coherence image was obtained by averaging those ten coherence images. The statistical thresholding using the surrogate data method was applied to select voxels with statistically significant values of coherence. Here, the number of surrogate datasets was set to 200, and the level of statistical significance α was set to 0.99. The results are shown in Fig. 8 in which the two central columns show the magnitude-coherence images, and the two rightmost columns show the imaginary-coherence images.

The results here show that the magnitude-coherence images are dominated by the seed blur. That is, for all three subjects, large blurred peaks are located near the seed voxels and no other peaks are seen in the magnitude-coherence images. On the contrary, the imaginary-coherence images are able to detect the right motor cortex and show the connectivity between the left and right motor cortices in the beta band. The seed blur that dominates the magnitude-coherence images is not seen in the imaginary-coherence images. These results effectively demonstrate that the artifactual seed blur does not exist when using imaginary coherence as the connectivity metric.

V. Discussion

In the analysis so far, we have ignored the interference terms $c_S(t)$ and $c_T(t)$. Here, we discuss the influence of these interference terms, and we use the expressions

$$\widehat{\sigma}_S = \bar{\sigma}_S + C_S \qquad \text{and} \qquad \widehat{\sigma}_T = \bar{\sigma}_T + C_T. \tag{23}$$

Here, C_S and C_T are the spectra of the interference terms, and $\bar{\sigma}_S$ and $\bar{\sigma}_S$ are the source spectra including only the leakage terms, which are defined such that $\bar{\sigma}_S = \sigma_S + d_1\sigma_T$ and $\bar{\sigma}_T = \sigma_T + d_2\sigma_S$. We assume that the interference spectra are independent from the source spectra, i.e., the relationships, $\langle \bar{\sigma}_T C_T^* \rangle = 0$, $\langle \bar{\sigma}_T C_S^* \rangle = 0$, $\langle \bar{\sigma}_S C_T^* \rangle = 0$, and $\langle \bar{\sigma}_S C_S^* \rangle = 0$, hold.

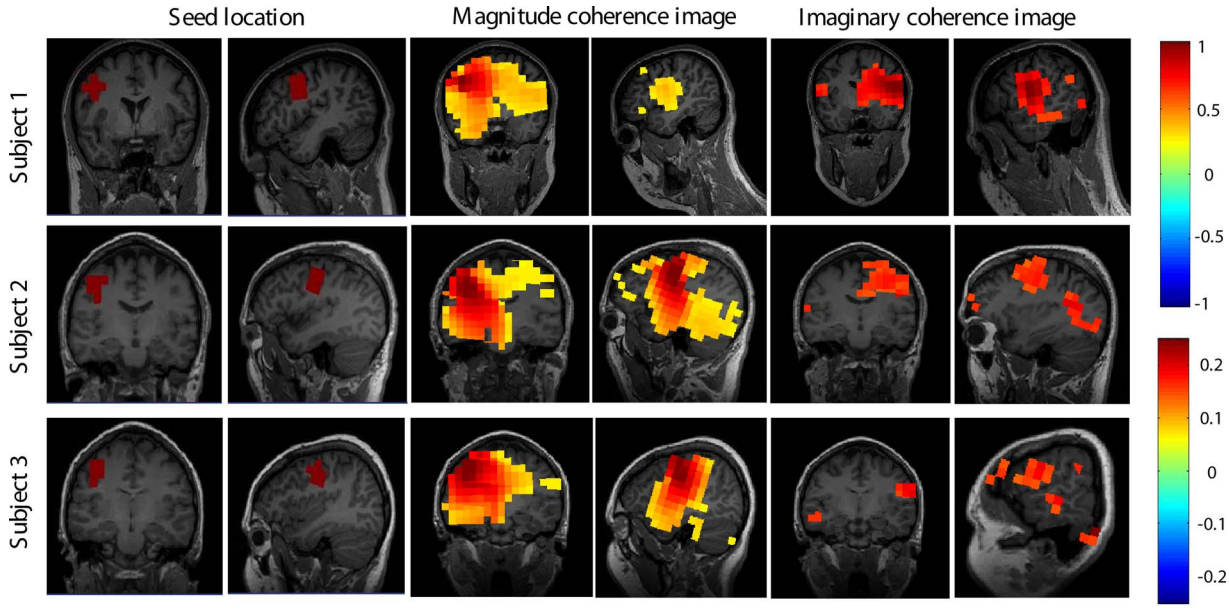

Fig. 8. Results of imaging beta-band coherence between the left and right primary motor cortices. The coherence images were obtained using the resting-state MEG data, and results for three subjects are shown. In each of the three pair of columns, a coronal view is presented on the left, and a sagittal view on the right. The two leftmost columns show the ten seed voxels in the precentral gyrus. The two middle columns show the magnitude-coherence images. The two rightmost columns show the imaginary-coherence images. The value of magnitude coherence is color-coded according to the upper color bar and the value of imaginary coherence to the lower color bar. The results from the first, second, and third subjects are, respectively, shown in the upper, middle, and bottom rows.

Then, using (23), the cross spectrum $\langle \widehat{\sigma}_T \widehat{\sigma}_S^* \rangle$ is expressed as

$$\langle \widehat{\sigma}_T \widehat{\sigma}_S^* \rangle = \langle \bar{\sigma}_T \bar{\sigma}_S^* \rangle + \langle C_T C_S^* \rangle \tag{24}$$

where $\langle C_T C_S^* \rangle$ indicates the spurious component due to the interference terms. The aforementioned equation indicates that the spurious component caused by the interference terms is additive to that caused from the leakage terms. Taking the imaginary part of both sides of (24), we derive

$$\Im\left(\langle \widehat{\sigma}_T \widehat{\sigma}_S^* \rangle\right) = \Im\left(\langle \bar{\sigma}_T \bar{\sigma}_S^* \rangle\right) + \Im\left(\langle C_T C_S^* \rangle\right). \tag{25}$$

If $\langle C_T C_S^* \rangle$ is real valued, we have $\Im\left(\langle \widehat{\sigma}_T \widehat{\sigma}_S^* \rangle\right) = \Im\left(\langle \bar{\sigma}_T \bar{\sigma}_S^* \rangle\right)$, and taking the imaginary part removes $\langle C_T C_S^* \rangle$.

To further investigate what scenarios make $\langle C_T C_S^* \rangle$ real valued, we must take the property of inverse algorithms into consideration. We assume that the voxel time courses are estimated using a spatial filter with real-valued weight vectors.[2] Under this assumption, the interference time courses $c_S(t)$ and $c_T(t)$ are expressed as $c_S(t) = \boldsymbol{w}^T(\boldsymbol{r}_S)\boldsymbol{b}_I(t)$ and $c_T(t) = \boldsymbol{w}^T(\boldsymbol{r}_T)\boldsymbol{b}_I(t)$, where $\boldsymbol{w}(\boldsymbol{r}_S)$ and $\boldsymbol{w}(\boldsymbol{r}_T)$ are real-valued weight vectors of the spatial filter at the seed and the target locations, respectively, and $\boldsymbol{b}_I(t)$ is the sensor recordings due to the interference and sensor noise.

By Fourier transforming $c_S(t)$ and $c_T(t)$, we obtain $C_S(f) = \boldsymbol{w}^T(\boldsymbol{r}_S)\boldsymbol{\beta}_I(f)$ and $C_T(f) = \boldsymbol{w}^T(\boldsymbol{r}_T)\boldsymbol{\beta}_I(f)$, where $\boldsymbol{\beta}_I(f)$ is the Fourier transform of $\boldsymbol{b}_I(t)$. The cross spectrum $\langle C_T C_S^* \rangle$ is, thus, expressed as

$$\langle C_T C_S^* \rangle = \boldsymbol{w}^T(\boldsymbol{r}_T)\langle \boldsymbol{\beta}_I(f)\boldsymbol{\beta}_I^H(f)\rangle \boldsymbol{w}(\boldsymbol{r}_S) \tag{26}$$

where the superscript H indicates the Hermitian transpose (the complex conjugation plus matrix transpose).

[2]Most of existing spatial filters including the narrow-band adaptive spatial filter used in our experiments employ real-valued weight vectors.

Since the weight $\boldsymbol{w}(\boldsymbol{r})$ is assumed to be a real-valued vector, in order for $\langle C_T C_S^* \rangle$ to be real valued, the matrix $\langle \boldsymbol{\beta}_I(f)\boldsymbol{\beta}_I^H(f)\rangle$ should be real valued. The diagonal elements of $\langle \boldsymbol{\beta}_I(f)\boldsymbol{\beta}_I^H(f)\rangle$ are real valued. The (j,k)th off-diagonal element of this matrix is given by

$$\langle \beta_I^{(j)}(f)\beta_I^{(k)*}(f)\rangle = \int_{-\infty}^{\infty} R_I^{(j,k)}(\tau)e^{-2\pi i f \tau} d\tau \tag{27}$$

where $\beta_I^{(j)}(f)$ and $\beta_I^{(k)}(f)$ is the jth and kth elements of $\boldsymbol{\beta}_I(f)$, respectively. Here, $R_I^{(j,k)}(\tau)$ is the cross correlation defined as

$$R_I^{(j,k)}(\tau) = \int_{-\infty}^{\infty} b_I^{(j)}(t) b_I^{(k)}(t+\tau) dt \tag{28}$$

where $b_I^{(j)}(t)$ and $b_I^{(k)}(t)$ are the jth and the kth elements of $\boldsymbol{b}_I(t)$, respectively. Note that since $\boldsymbol{b}_I(t)$ is real valued, $R_I^{(j,k)}(\tau)$ is real valued.

In general, we can decompose $R_I^{(j,k)}(\tau)$ into

$$R_I^{(j,k)}(\tau) = R_E^{(j,k)}(\tau) + R_O^{(j,k)}(\tau) \tag{29}$$

where $R_E^{(j,k)}(\tau)$ is an even function and $R_O^{(j,k)}(\tau)$ is an odd function. Since the Fourier transform of a real even function is real valued, the real part of $\langle \beta_I^{(j)}(f)\beta_I^{(k)*}(f)\rangle$ is caused from the even-function component $R_E^{(j,k)}(\tau)$, and the imaginary part of $\langle \beta_I^{(j)}(f)\beta_I^{(k)*}(f)\rangle$ is caused from the odd-function component $R_O^{(j,k)}(\tau)$.

Assuming that the interference $\boldsymbol{b}_I(t)$ is a stationary process, we have the relationship $R_I^{(j,k)}(-\tau) = R_I^{(k,j)}(\tau) = R_I^{(j,k)}(\tau)$. Thus, $R_I^{(j,k)}(\tau)$ is an even function and $\langle C_T C_S^* \rangle$ is real valued. As a result, taking the imaginary part of $\langle C_T C_S^* \rangle$ can effectively remove the spurious cross spectrum $\langle C_T C_S^* \rangle$. However,

when $\boldsymbol{b}_I(t)$ deviates from a stationary process, $R_O^{(j,k)}(\tau)$ may become significant, and using the imaginary coherence may be less effective in removing $\langle C_T C_S^* \rangle$.

Imaginary coherence has already been applied to MEG source-space connectivity analysis, and resting-state functional connectivity mappings have been performed using imaginary coherence for schizophrenia patients [21] and for brain tumor patients [7], [22]. In these publications, however, the primary scope has been on the clinical implications of the connectivity results and no rigorous arguments have been presented regarding the choice of imaginary coherence.

This paper has presented detailed theoretical analysis on the properties of imaginary coherence in source-space coherence imaging. Our analysis and experiments show that magnitude-coherence images are confounded by the spurious coherence caused by the leakage properties of the inverse algorithm. The spurious coherence is manifested as the seed blur, which is an artifactual large peak around the seed voxel in the resulting coherence images. This paper proposes the use of the imaginary coherence to remove this seed blur, and presents a detailed theoretical analysis that explains how the use of imaginary coherence leads to the removal of the seed blur. The effectiveness of using imaginary coherence has been validated by our computer simulation and experiments using resting-state MEG data.

It should be pointed out that the effectiveness of using imaginary coherence holds, regardless of the source imaging algorithm used to estimate voxel time courses. The use of the adaptive spatial filter in our computer simulation and the experiments was mainly due to the convenience in our software developments. It should, however, be emphasized that the use of imaginary coherence cannot retrieve source activities the source imaging algorithm fails to reconstruct.

Our analysis shows that the estimated imaginary coherence has the amplitude bias due to the leakage of an imaging algorithm employed. Recently, Brookes *et al.* [23] reported that the length of a time window for coherence computation also affects the amplitude of estimated coherence. Further studies are needed to examine whether other factors exist that also produce the amplitude bias, and whether such amplitude biases in imaginary coherence are really problematic for the estimation of functional connectivity with this metric.

ACKNOWLEDGMENT

We would like to thank S. Honma and A. Findlay for their help in measuring the resting-state MEG data.

REFERENCES

[1] Z. Liu, M. Fukunaga, J. A. de Zwart, and J. H. Duyn, "Large-scale spontaneous fluctuations and correlations in brain electrical activity observed with magnetoencephalography," *NeuroImage*, vol. 51, pp. 102–111, 2010.

[2] T. Montez, S. Poil, B. F. Jones, I. Manshanden, J. P. A. Verbunt, B. W. van Dijk, A. B. Brussaard, A. van Ooyen, C. J. Stam, P. Scheltens, and K. Linkenkaer-Hansen, "Altered temporal correlations in parietal alpha and prefrontal theta oscillations in early stage Alzheimer disease," *Proc. Nat. Acad. Sci. U.S.A.*, vol. 106, pp. 1614–1619, 2009.

[3] A. P. Georgopoulos, E. Karageorgiou, A. C. Leuthold, S. M. Lewis, J. K. Lynch, A. A. Alonso, Z. Aslam, A. F. Carpenter, A. Georgopoulos, L. S. Hemmy, I. G. Koutlas, F. J. Langheim, J. R. McCarten, S. E. McPherson, J. V. Pardo, P. J. Pardo, G. J. Parry, S. J. Rottunda, B. M. Segal, S. R. Sponheim, J. J. Stanwyck, M. Stephane, and J. J. Westermeyer, "Synchronous neural interactions assessed by magnetoencephalography: A functional biomarker for brain disorders," *J. Neural Eng.*, vol. 4, pp. 349–355, 2007.

[4] J.-M. Schoffelen and J. Gross, "Source connectivity analysis with MEG and EEG," *Human Brain Mapping*, vol. 30, pp. 1857–1865, 2009.

[5] J. Gross, J. Kujara, M. Hämäläinen, L. Timmermann, A. Schnitzler, and R. Salmelin, "Dynamic imaging of coherent sources: Studying neural interactions in the human brain," *Proc. Nat. Acad. Sci. U.S.A.*, vol. 98, pp. 694–699, 2001.

[6] P. Belardinelli, L. Ciancetta, M. Staudt, V. Pizzella, A. Londei, N. B. G. L. Romani, and C. Braun, "Cerebro-muscular and cerebro-cerebral coherence in patients with pre- and perinatally acquired unilateral brain lesions," *NeuroImage*, vol. 37, pp. 1301–1314, 2007.

[7] A. G. Guggisberg, S. M. Honma, A. M. Findlay, S. S. Dalal, H. E. Kirsch, M. S. Berger, and S. S. Nagarajan, "Mapping functional connectivity in patients with brain lesions," *Ann. Neurol.*, vol. 63, pp. 193–203, 2007.

[8] D. Mantini, M. G. Perucci, C. D. Gratta, G. L. Romani, and M. Corbetta, "Electrophysiological signatures of resting state networks in the human brain," *Proc. Nat. Acad. Sci. U.S.A.*, vol. 104, pp. 13170–13175, 2007.

[9] L. Astolfi and F. Babiloni, *Estimation of Cortical Connectivity in Humans*. New York: Morgan & Claypool Publishers, 2008.

[10] W. H. R. Miltner, C. Braun, M. Arnold, H. Witte, and E. Taub, "Coherence of gamma-band EEG activity as a basis for associative learning," *Nature*, vol. 397, pp. 434–436, 1999.

[11] P. L. Nunez, R. Srinivasan, A. F. Westdorf, R. S. Wijesinghe, D. M. Tucker, R. B. Silberstein, and P. J. Cadusch, "EEG coherency I: Statistics, reference electrode, volume conduction, Laplacians, cortical imaging, and interpretation at multiple scale," *Electroencephalogr. Clin. Neurophysiol.*, vol. 103, pp. 499–515, 1997.

[12] K. Sekihara and S. S. Nagarajan, *Adaptive Spatial Filters for Electromagnetic Brain Imaging*. Berlin, Germany: Springer-Verlag, 2008.

[13] G. Nolte, O. B. L. Wheaton, Z. Mari, S. Vorbach, and M. Hallett, "Identifying true brain interaction from EEG data using the imaginary part of coherency," *Clin. Neurophysiol.*, vol. 115, pp. 2292–2307, 2004.

[14] J. Theiler, S. Eubank, A. Longtin, B. Galdrikian, and J. D. Farmer, "Testing for nonlinearlity in time series: The method of surrogate data," *Physica D*, vol. 58, pp. 77–94, 1992.

[15] L. Faes, G. D. Pinna, A. Porta, R. Maestri, and G. Nollo, "Surrogate data analysis for assessing the significance of the coherence function," *IEEE Trans. Biomed. Eng.*, vol. 51, no. 7, pp. 1156–1166, Jul. 2004.

[16] Y. Benjamini and Y. Hochberg, "Controlling the false discovery rate: A practical and powerful approach to multiple testing," *J. Roy. Statist. Soc. B*, vol. 57, pp. 289–300, 1995.

[17] T. E. Nichols and S. Hayasaka, "Controlling the familywise error rate in functional neuroimaging: A comparative review," *Statist. Methods Med. Res.*, vol. 12, pp. 419–446, 2003.

[18] J. Sarvas, "Basic mathematical and electromagnetic concepts of the biomagnetic inverse problem," *Phys. Med. Biol.*, vol. 32, pp. 11–22, 1987.

[19] S. S. Dalal, A. G. Guggisberg, E. Edwards, K. Sekihara, A. M. Findlay, R. T. Canolty, M. S. Berger, R. T. Knight, N. M. Barbaro, H. E. Kirsch, and S. S. Nagarajan, "Five-dimensional neuroimaging: Localization of the time-frequency dynamics of cortical activity," *NeuroImage*, vol. 40, pp. 1686–1700, 2008.

[20] S. S. Dalal, J. M. Zumer, A. G. Guggisberg, M. Trumpis, D. D. E. Wong, K. Sekihara, and S. S. Nagarajan, "MEG/EEG source reconstruction, statistical evaluation, and visualization with NUTMEG," *Comput. Intell. Neurosci.*, art. 75893, 2011.

[21] L. B. Hinkley, J. P. Owen, M. Fisher, A. M. Findlay, S. Vinogradov, and S. S. Nagarajan, "Cognitive impairments in schizophrenia as assessed through activation and connectivity measures of magnetoencephalography (MEG) data," *Frontiers Human Neurosci.*, vol. 3, art. 73, 2009.

[22] J. Martino, S. M. Honma, A. F. Findlay, A. G. Guggisberg, M. S. Berger, H. E. Kirsch, and S. S. Nagarajan, "Resting functional connectivity in patients with brain tumors in eloquent areas," *Ann. Neurol.*, vol. 69, pp. 521–532, 2011.

[23] M. J. Brookes, J. R. Hale, J. M. Zumer, C. M. Stevenson, S. T. Francis, G. R. Barnes, J. P. Owen, P. G. Morris, and S. S. Nagarajan, "Measuring functional connectivity using MEG: Methodology and comparison with fcMRI," *NeuroImage*, vol. 56, pp. 1082–1104, 2011.

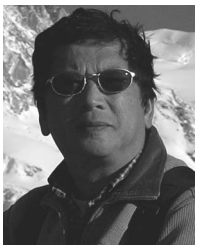

Kensuke Sekihara (F'09) received the M.S. and Ph.D. degrees from the Tokyo Institute of Technology, Tokyo, Japan, in 1976 and 1987, respectively.

From 1976 to 2000, he was with Central Research Laboratory, Hitachi, Ltd., Tokyo, Japan. From 1985 to 1986, he was a Visiting Research Scientist at Stanford University, Stanford, CA, and from 1991 to 1992, he was at Basic Development, Siemens Medical Engineering, Erlangen, Germany. From 1996 to 2000, he was with "Mind Articulation" research project sponsored by Japan Science and Technology Corporation. He is currently a Professor in the Department of Systems Design and Engineering, Tokyo Metropolitan University, Tokyo, Japan. He is the author of the book entitled *AdaptiveSpatial Filters for Electromagnetic Brain Imaging* (1st ed. New York: Springer, 2008). His research interests include the electromagnetic source imaging, reconstruction and inverse methods, multidimensional signal processing, and statistical signal processing, especially their application to functional source imaging.

Dr. Sekihara is a member of the IEEE Medicine and Biology Society and the IEEE Signal Processing Society. He is a Fellow of the International Society of Functional Source Imaging.

Julia P. Owen received the B.S.E. degree from The Cooper Union, New York, NY, in 2003, and the Ph.D. degree in bioengineering from the Joint Program in Bioengineering, University of California, San Francisco (UCSF), and University of California, Berkeley, in 2011.

She did her graduate research with Dr. Nagarajan at the Biomagnetic Imaging Laboratory, UCSF. Her research interests include the development of source localization algorithms for magnetoencephalography and their use with functional connectivity metrics.

Stephen Trisno received the B.S. degree in bioengineering from the University of California, Berkeley.

In the summer of 2010, he started his research as an Undergraduate Researcher at the Biomagnetic Imaging Laboratory, University of California, San Francisco. He aspires to go to medical school after completing his degree.

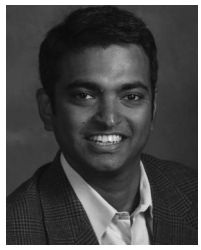

Srikantan S. Nagarajan (SM'09) received the M.S and Ph.D. degrees in biomedical engineering from Case Western Reserve University, Cleveland, OH.

He was a Postdoctoral Fellow at the Keck Center for Integrative Neuroscience, University of California, San Francisco (UCSF). He is currently a Professor in the Department of Radiology and Biomedical Imaging and the Department of Bioengineering and Therapeutic Sciences, UCSF, and a member of the Joint Graduate Program in Bioengineering, UCSF/University of California, Berkeley. His research interests include the areas of neural engineering and machine learning, better understanding neural mechanisms of sensorimotor learning and speech motor control, and developing algorithms for improved functional brain imaging, biomedical signal processing, and brain–computer interfaces.